

An OpenFOAM Framework to Model Thermal Bubble-Driven Micro-Pumps

## An OpenFOAM Framework to Model Thermal Bubble-Driven Micro-Pumps

 B. Hayes,<sup>1</sup> G. L. Whiting,<sup>1</sup> and R. MacCurdy<sup>1, a)</sup>
*Paul M. Rady Department of Mechanical Engineering, University of Colorado Boulder, Boulder, Colorado 80309, USA*

(Dated: 3 June 2023)

Thermal bubble-driven micro-pumps (also known as inertial pumps) are an upcoming micro-pump technology that can be integrated directly into micro/mesofluidic channels to displace fluid without moving parts. These micro-pumps are high power resistors that locally vaporize a thin layer of fluid above the resistor surface to form a high pressure vapor bubble which performs mechanical work. Despite their geometric simplicity, thermal bubble-driven micro-pumps are complex to model due to the multiphysics couplings of Joule heating, thermal bubble nucleation, phase change, and multiphase flow. As such, most simulation approaches simplify the physics by neglecting Joule heating, nucleation, and phase change effects as done in this study. To date, there are no readily available, reduced physics open source modeling tools that can resolve both pre-collapse (defined as when the bubble is expanding and collapsing) and post-collapse (defined as when the bubble has re-dissolved back into the subcooled fluid) bubble and flow dynamics. In this study, an OpenFOAM framework for modeling thermal bubble-driven micro-pumps is presented, validated, and applied. The developed OpenFOAM model agrees with both experimental data and commercial computational fluid dynamics (CFD) software, FLOW-3D. Additionally, we assess the shape of the transient velocity profile during a pump cycle for the first time and find that it varies substantially from theoretical Poiseuille flow during pre-collapse but is within 25% of the theoretical flow profile during post-collapse. We find that this deviation is due to flow never becoming fully developed during each pump cycle. We envision the developed OpenFOAM framework as an open source CFD toolkit for microfluidic designers to simulate devices with thermal bubble-driven micro-pumps.

### I. INTRODUCTION

The ability to precisely move fluid in a microchannel is critical to any microfluidic system. In the last few decades, there have been a wide variety of micro-pumps based on a range of physics: electrostatic<sup>1,2</sup>, magnetic<sup>3</sup>, centrifugal<sup>4</sup>, peristaltic<sup>5</sup>, piezoelectric<sup>6</sup>, capillary action<sup>7</sup>, and thermal bubbles<sup>8</sup>. These micro-pumps can be active, requiring energy input, or passive. However, the wide variety of micro-pump sources presents a major challenge when it comes to standardization and commercialization of microfluidic systems as often the infrastructure to mass produce microfluidic devices does not exist<sup>9</sup>. Thus, there is a need for a micro-pump source in microfluidics that is (a) reliable, (b) internal, (c) simple and mass producible, and (d) scalable. A promising solution is thermal bubble-driven micro-pumps. Thermal bubble-driven micro-pumps (also known as inertial pumps) are an emerging micro-pump technology with no moving parts that can be integrated directly into microfluidic channels, are scalable, and leverage existing semiconductor mass fabrication infrastructure<sup>8</sup>. Based on thermal inkjet (TIJ) technology, thermal bubble-driven micro-pumps consist of a micro-resistor which locally vaporizes an interfacial layer of fluid at the resistor's surface during a microsecond heating pulse to create a vapor bubble that performs mechanical work<sup>10,11</sup>. Beyond fluid pumping, these micro-pumps have been used for mixing<sup>12</sup>, fluid sorting/routing<sup>13</sup>, cell lysis<sup>14</sup>, and even micro-mechanical actuation<sup>15,16</sup> demonstrating the versatility of this technology. As such, these micro-pumps

show great promise in enabling standardization and commercialization of true "lab-on-a-chip" devices.

Although geometrically simple, the physics behind thermal bubble-driven micro-pumps are complex. During a microsecond heating pulse, fluid is heated to near its critical temperature (300 °C for water) at heating rates of 100 °C/μs<sup>10</sup>. This thermal impulse results in metastable boiling at the resistor's surface which forms a single high pressure vapor bubble<sup>17</sup>. If the resistor is placed asymmetrically in a channel between two reservoirs, the expansion-collapse dynamics of the vapor bubble result in unidirectional flow from the short to long leg of the channel<sup>11</sup>, where "short leg" refers to the shorter channel segment from the reservoir to the center of the resistor as shown in figure 1b. Consider a single vapor bubble expansion-collapse event, figure 1a-c. After nucleation, the high pressure vapor bubble expands, and fluid is forced into the reservoirs. Fluid is accelerated faster in the short leg than the long leg of the channel due to inertia; as such, momentum dissipation is faster on the short leg of the channel. As the vapor bubble expands and performs work on the fluid, it loses pressure until its internal pressure becomes sub-atmospheric. After reaching its maximum expansion extent, the vapor bubble collapses and the channel refills with liquid. The short leg refills faster than the long leg of the channel which results in fluid in the short leg having a greater momentum at the point of bubble collapse. This momentum imbalance drives fluid flow in the direction of short to long leg of the channel until fluid is eventually brought to rest by viscosity.

In practice, thermal bubble-driven micro-pumps built using semiconductor fabrication workflows have long lead

<sup>a)</sup>Electronic mail: maccurdy@colorado.edu, corresponding author

times on the order of weeks/months. Although research and development (R&D) work has demonstrated simplified experimental workflows to rapidly prototype devices in a matter of hours/days<sup>18</sup>, manual fabrication approaches are ill-suited for large design optimization studies needed for commercial devices. In this case, computational fluid dynamic (CFD) models can be a useful tool in understanding, designing, and optimizing microfluidic systems with thermal bubble-driven micro-pumps. Full multiphysics CFD modeling requires coupling of Joule heating, thermal bubble nucleation, phase change, and multiphase flow. Numerous multiphysics commercial software such as ANSYS<sup>19</sup>, FLOW-3D<sup>20</sup>, and COMSOL<sup>21</sup> as well as academic codes<sup>22</sup> can accurately simulate the full multiphysics of these thermal bubble-driven actuators, but with a high computational cost<sup>23</sup> making full multiphysics models ill-suited for large design optimization studies. Additionally, commercial software is expensive which often limits accessibility to researchers. As such, there have been a variety of approaches to simplify modeling of thermal bubble-driven micro-pump ranging from one-dimensional (1D) models to reduced physics three-dimensional (3D) CFD models. For the former, Prosperetti et al. and Kornilovitch et al. first independently proposed and validated reduced order 1D models in which bubble and flow physics are captured through tracking the evolution of a 1D interface subjected to a pressure initial condition that drives bubble expansion<sup>11,24–27</sup>. While 1D models are highly useful for rapid evaluation of design spaces using thermal bubble-driven micro-pumps and can even account for more complicated temperature dependent pumping effects<sup>28</sup>, reduced order 1D models inherently cannot capture 3D bubble and flow physics that must be resolved for more complex channel geometries, such as a Y-channel or 3D tapered channels. In these cases, 3D CFD is required. The most common approach used to simplify full thermal bubble multiphysics is to assume at the onset that a thin vapor layer has formed and to apply pressure initial and boundary conditions on the vapor region. This approach was first developed by Asai et al. and has been well studied and validated to capture both bubble and flow dynamics in TIJ devices<sup>29</sup>. Later, Tan et al. developed an internal 3D CFD code, CFD3, for modeling TIJ droplet ejection dynamics as well as thermal bubble-driven micro-pump dynamics based on the volume of fluid (VOF) approach and simplifying thermal bubble nucleation to a seed layer of vapor undergoing polytropic gas expansion<sup>30</sup>. Neglecting thermal bubble nucleation allows for significant computational speed-up making reduced physics 3D CFD approaches a viable option for parameter and design optimization of microfluidic systems with thermal bubble-driven micro-pumps.

While internal CFD codes developed by individual academic groups, such as that by Asai et al., and corporations, such as that by Tan et al. of Hewlett-Packard Inc., have been verified and validated to accurately model the thermal bubble actuation process, little research to date has utilized more accessible, open source CFD codes. However, the availability of open source CFD codes for thermal bubble-driven micro-

pumps is an important step to enable wide spread use of this micro-pump technology. In this study, we present a framework which utilizes the open source CFD code *OpenFOAM* to model bubble and flow physics of both pre-collapse, defined as when the bubble is expanding and collapsing in a channel, and post-collapse, defined as when the bubble is re-absorbed back into the subcooled fluid, micro-pump stages. To date, OpenFOAM has been successfully utilized to model only the pre-collapse stage of thermal bubble-driven micro-pumps by seeding an initial vapor layer of a specific volume, pressure, and temperature and letting the compressible, two-phase solver *compressibleInterFoam* evolve the bubble and flow dynamics<sup>31–34</sup>. During post-collapse, the vapor bubble must be re-absorbed back into the subcooled fluid. This requires mass transport which is not available in the OpenFOAM *compressibleInterFoam* solver. In this work, we extend the standard OpenFOAM *compressibleInterFoam* solver to capture both pre-collapse and post-collapse bubble and flow dynamics using heuristics based on thermal bubble-driven micro-pump physics. We validate our OpenFOAM framework against experimental data as well as commercial CFD software, FLOW-3D. Lastly, we demonstrate the application of our OpenFOAM framework to analyze the transient velocity profile during a pump cycle. To our knowledge, this is the first readily available, open source CFD framework capable of handling both pre-collapse and post-collapse bubble and flow dynamics. We envision the developed OpenFOAM framework as an open source toolkit for microfluidic designers to understand and simulate 3D bubble and flow physics of devices using thermal bubble-driven micro-pumps.

## II. OPENFOAM COMPUTATIONAL MODEL

The OpenFOAM *compressibleInterFoam* solver was used to solve continuity, momentum, energy, state, and volume fraction equations that describe bubble and flow dynamics of thermal bubble-driven micro-pumps. We note that the *compressibleInterFoam* solver does not account for mass transfer; as such, true thermal bubble nucleation and post-collapse dissolution cannot be simulated with the built-in solver. Instead, we develop heuristics, defined in section II B, to accurately simulate thermal bubble-driven micro-pumps based on pre-collapse and post-collapse physics. OpenFOAM model files are provided in the Matter Assembly Computation Lab's ([www.matterassembly.org](http://www.matterassembly.org)) public github repository (<https://github.com/MacCurdyLab/An-OpenFOAM-Framework-to-Model-Thermal-Bubble-Driven-Micro-Pumps>) as well as the supplemental material.

### A. Model Description

Bubble and flow dynamics are modeled using the 2-phase compressible, laminar, sharp interface fluid solver *compressibleInterFoam* in OpenFOAM v10. Liquid and vapor phases are captured using the volume of fluid (VOF) phase field method with interface compression<sup>35</sup> for each phase scalar

field denoted by  $\alpha$ . Specifically,  $\alpha \in [0, 1]$  for each cell element. A mixture density ( $\rho$ ) and viscosity ( $\mu$ ) is used by weighting the phases within each cell element where

$$\rho = \rho_{liquid}\alpha + \rho_{vapor}(1 - \alpha) \quad (1)$$

and

$$\mu = \mu_{liquid} + \mu_{vapor}(1 - \alpha). \quad (2)$$

The compressible Navier-Stokes equations are then solved as follows accounting for interfacial tension forces<sup>36</sup>:

$$\frac{\partial \rho}{\partial t} + \nabla \cdot (\rho \mathbf{u}) = 0 \quad (3)$$

$$\begin{aligned} \frac{\partial (\rho \mathbf{u})}{\partial t} + \nabla \cdot (\rho \mathbf{u} \mathbf{u}) = & -\nabla \left( p + \frac{2}{3} \mu \nabla \cdot \mathbf{u} \right) \\ & + \nabla \cdot (\mu (\nabla \mathbf{u} + (\nabla \mathbf{u})^T)) \\ & + \mathbf{F}_{st} + \mathbf{F}_g \end{aligned} \quad (4)$$

$$\begin{aligned} \frac{\partial (\rho T)}{\partial t} + \nabla \cdot (\rho \mathbf{u} T) - \nabla \cdot (\mu T) = & -\left( \frac{\alpha}{C_{v,liquid}} + \frac{1 - \alpha}{C_{v,vapor}} \right) \\ & \times \left( \frac{\partial (\rho k)}{\partial t} + \nabla \cdot (\rho \mathbf{u} k) \right. \\ & \left. + \nabla \cdot (\rho \mathbf{u}) \right) \end{aligned} \quad (5)$$

where  $\mathbf{u}$  is the velocity field,  $p$  is the pressure,  $\mathbf{F}_{st}$  is the surface tension force, and  $\mathbf{F}_g$  is the gravitational body force,  $T$  is the temperature,  $C_{v,liquid}$  and  $C_{v,vapor}$  are the heat capacities of liquid and vapor phases respectively, and  $k$  is the kinetic energy per unit mass,  $k = |\mathbf{u}|^2/2$ . The surface tension force is given by

$$\mathbf{F}_{st} = \gamma \left( \nabla \cdot \left( \frac{\nabla \alpha}{|\nabla \alpha|} \right) \right) \nabla \alpha \quad (6)$$

where  $\gamma$  is the surface tension. The gravitational force is given by

$$\mathbf{F}_g = \rho \mathbf{g} \quad (7)$$

where  $\mathbf{g}$  is the gravitational acceleration. These equations are solved using the multi-dimensional limiter for explicit solution (MULES) algorithm. An adjustable time step formulation based on the Courant–Friedrichs–Lewy (CFL) criterion is utilized in the forward Euler temporal numerical scheme with a maximum CFL number set to 0.50 to ensure stability. Phases are tracked by solving the phase fraction advected through each fluid with interface compression:

$$\frac{\partial \alpha}{\partial t} + \nabla \cdot (\alpha \mathbf{u}) + \nabla \cdot (U_r \alpha (1 - \alpha)) = 0. \quad (8)$$

$U_r$  is the numerical applied velocity field used to compress the interface given by

$$U_r = C_\alpha \frac{\nabla \alpha}{|\nabla \alpha|} \quad (9)$$

where  $C_\alpha$  is a binary term  $\{0, 1\}$  to toggle interface compression<sup>37</sup>. State equations for the vapor and liquid phases, which is modeled by air and water respectively in this simulation, are defined by

$$\rho_a = \frac{1}{R_a T} p_a \quad (10)$$

$$\rho_w = \frac{1}{R_w T} p_w + \rho_{w,o} \quad (11)$$

where  $\rho_a$  is the density of air,  $R_a$  is the universal constant for air,  $p_a$  is the pressure of air,  $\rho_w$  is the density of water,  $R_w$  is the universal constant for water,  $p_w$  is the pressure of water, and  $\rho_{w,o}$  is the initial density of water.

## B. Pre-Collapse and Post-Collapse Heuristics

Full modeling of thermal bubble nucleation couples heat transfer with the Clausius-Clapeyron equation,

$$P_{sat}(T) = P_i \cdot e^{\frac{1}{T_{exp}} \left( \frac{1}{T_i} - \frac{1}{T} \right)} \quad (12)$$

$$T_{exp} = (\gamma - 1) \frac{C_v}{\Delta H_v} \quad (13)$$

where  $P_i$  and  $T_i$  are pressure and temperature values at a point on the saturation vapor pressure curve,  $\gamma$  is the ratio of vapor specific heats  $\left( \frac{C_p}{C_v} \right)$ ,  $C_p$  is the vapor specific heat at constant pressure,  $C_v$  is the vapor specific heat at constant volume, and  $\Delta H_v$  is the latent heat of vapor. This coupling is used to predict the initial bubble pressure based off of the liquid temperature at the onset of nucleation, as performed in FLOW-3D<sup>20,23</sup>. In addition, mass transport is coupled to account for vapor dissolution upon bubble collapse. These couplings are computationally expensive. As such, we simplify the model with the following assumptions, also displayed graphically in figure 1:

1. Thermal bubble nucleation is represented by an initial vapor layer of set thickness, pressure, and temperature with area  $W_r \times L_r$  where  $W_r$  and  $L_r$  are the resistor width and length respectively
2. At the maximum expansion extent, all vapor cells are assigned a sub-atmospheric collapse pressure,  $p = 0.03 p_o$  where  $p_o$  is atmospheric pressure, to allow the vapor bubble to uniformly collapse
3. When the vapor bubble short leg collides with that of the long leg, all vapor cells are turned back into liquid to simulate vapor “dissolution” upon bubble collapse.

Assumption 1 is commonly used to simplify thermal bubble nucleation models<sup>29,30</sup> since the metastable boiling nucleation process rapidly forms a high pressure vapor blanket across the resistor surface after which the vapor bubble grows due to inertia<sup>10,17</sup>. As the vapor bubble expands, its internal pressure decreases until the surrounding fluid pressure causes the vapor bubble to collapse. In assumption 2, the vapor bubble pressure at max expansion is set to a sub-atmospheric pressure,  $p = 0.03p_o$ , to ensure even collapse of the vapor bubble, as done by Hongchen et al.<sup>31</sup>. Assumption 3 captures the “dissolution” process upon collapse of the vapor bubble and is based on post-collapse physics, which is not captured by the approach put forth from Hongchen et al. Upon collapse, fluid in the short leg of the channel can be thought of as having an inelastic collision with fluid in the long leg of the channel. As such, turning all vapor cells into liquid at the point of collapse is representative of the fluid’s inelastic collision. This heuristic is crucial to the proposed OpenFOAM model as the *compressibleInterFoam* solver will never re-dissolve the vapor bubble back into the fluid since mass transport is not modeled.

### C. Automatic Heuristic Application

To properly apply the aforementioned pre-collapse and post-collapse heuristics, the developed OpenFOAM model requires input of the initial vapor layer thickness, pressure, and temperature as well as expansion time, defined as the time when the vapor bubble reaches its maximum extent, and collapse time, defined as the time when the vapor bubble fully collapses. However, the expansion and collapse times are dependent on the initial vapor layer parameters as well as the resistor location in a channel and channel geometry. As such, the expansion and collapse times must be computed during simulation run time.

To do so, we divide the simulation into three phases: (1) computation of the expansion time, (2) computation of the collapse time, and (3) computation of the full bubble and fluid dynamics. In phase 1, the simulation is set to run with the input of initial vapor layer thickness, pressure, and temperature for a given resistor of width  $x$  length,  $W_r \times L_r$ , shown in figure 1a. Cut planes 1-4 are used to monitor the flow rate and velocity profile throughout the channel. A sampling plane spanning the length of the channel is placed at the resistor center shown in figure 1b. Monitoring the vapor bubble extents, the expansion time is taken as the time of maximum vapor bubble extent in the short leg of the channel, figure 1d. In phase 2, the simulation is reset with the calculated expansion time and the vapor bubble is let to evolve. An additional sampling plane spanning the channel cross-section is placed in the long leg of the channel to monitor the flow rate, cut plane 1 in figure 1a. The collapse time is determined by computing the gradient of the cumulative flow rate and finding the time at which the slope first changes from negative to positive which is indicative of collapse, figure 1c,e-f. Lastly, in phase 3, the simulation is reset with the calculated expansion and collapse times, and

the bubble and fluid dynamics are let to evolve for the full simulation run time.

### D. OpenFOAM Model Validation

The OpenFOAM reduced physics 3D CFD model requires experimental data to ensure proper initial bubble conditions. Once the bubble initial conditions are known for a given resistor design, these conditions are constant so long as the same resistor size and firing conditions are maintained. As such, we validate the developed OpenFOAM framework on a U-shaped channel geometry from the experimental work of Govyadinov et al.<sup>11</sup> in which a  $15 \times 33.5 \mu\text{m}^2$  resistor was placed  $43 \mu\text{m}$  from the channel reservoir. The channel had dimensions of  $L = 403 \mu\text{m}$ ,  $W = 22 \mu\text{m}$ , and  $H = 17 \mu\text{m}$ , see figure 4. The bubble initial conditions (thickness, pressure, and temperature) are found by performing a least-squares parameter optimization using the OpenFOAM cumulative flow rate, which we denote “volume displaced,” compared against experimental flow rate data<sup>11</sup>, see equation 14 where  $y_o$  is OpenFOAM volume displaced data and  $y_e$  is the experimental volume displaced data.

$$SSE = \sum_{i=1}^N (y_o^i - y_e^i)^2 \quad (14)$$

The sum squared error (SSE) is then computed for each  $i^{\text{th}}$  time step for all  $N$  total time steps. Using the automated heuristic solver, the initial bubble conditions after least-squares optimization were:  $t_b = 454 \text{ nm}$ ,  $p_b = 113p_o$ , and  $T_b = 557 \text{ K}$  where  $t_b$  is the initial vapor layer thickness,  $p_b$  is the initial bubble pressure,  $p_o$  is atmospheric pressure, and  $T_b$  is the initial bubble temperature. A  $1.25 \mu\text{m}$  grid resolution was used for the parameter optimization study and the minimum SSE was  $4.78 \text{ pL}^2$ . Figure 2 shows the cumulative flow rate of the fitted OpenFOAM model to FLOW-3D<sup>23</sup> and experimental data<sup>11</sup>. The OpenFOAM model is in excellent agreement with both FLOW-3D and experimental data. To assess the mesh dependency of the OpenFOAM model, we performed a mesh analysis study for  $0.625$ ,  $1.25$ , and  $2.5 \mu\text{m}$  grid cell resolutions. Figure 3 shows mesh convergence for  $0.625$  and  $1.25 \mu\text{m}$  grid cell resolutions; thus,  $0.625 \mu\text{m}$  grid cells were used in this study when higher grid resolution was needed while  $1.25 \mu\text{m}$  grid cells were used as a trade-off between accuracy and computational time.

Figure 4 compares experimental top-down bubble dynamics to both FLOW-3D and OpenFOAM simulation results at discrete time steps. The U-shaped channel geometry was matched with that from the experimental work of Govyadinov et al.<sup>11</sup> No-slip boundary conditions ( $\mathbf{u} = 0$ ) were applied to all boundaries except the bottom of the reservoir in which a static pressure boundary condition ( $p = p_o$ ) was applied. Our previous study<sup>23</sup> validated FLOW-3D bubble and flow dynamics against the U-shaped channel geometry used in this study and thus serves as a basis of comparison for the developed OpenFOAM framework. OpenFOAM top-down

This is the author's peer reviewed, accepted manuscript. However, the online version of record will be different from this version once it has been copyedited and typeset.

PLEASE CITE THIS ARTICLE AS DOI: 10.1063/5.0155615

*Accepted to Phys. Fluids 10.1063/5.0155615*

An OpenFOAM Framework to Model Thermal Bubble-Driven Micro-Pumps

5

bubble dynamics were in agreement with both experimental images and FLOW-3D results. Figure 5 compares side-view bubble dynamics of OpenFOAM and FLOW-3D. OpenFOAM side-view bubble dynamics were in good agreement with that of FLOW-3D. However, we note that during bubble collapse in the OpenFOAM model,  $t > 4 \mu\text{s}$ , the vapor bubble does not fully fill the channel height as in the FLOW-3D model.

This is the author's peer reviewed, accepted manuscript. However, the online version of record will be different from this version once it has been copyedited and typeset.  
PLEASE CITE THIS ARTICLE AS DOI: 10.1063/5.0155615

Accepted to Phys. Fluids 10.1063/5.0155615

An OpenFOAM Framework to Model Thermal Bubble-Driven Micro-Pumps

6

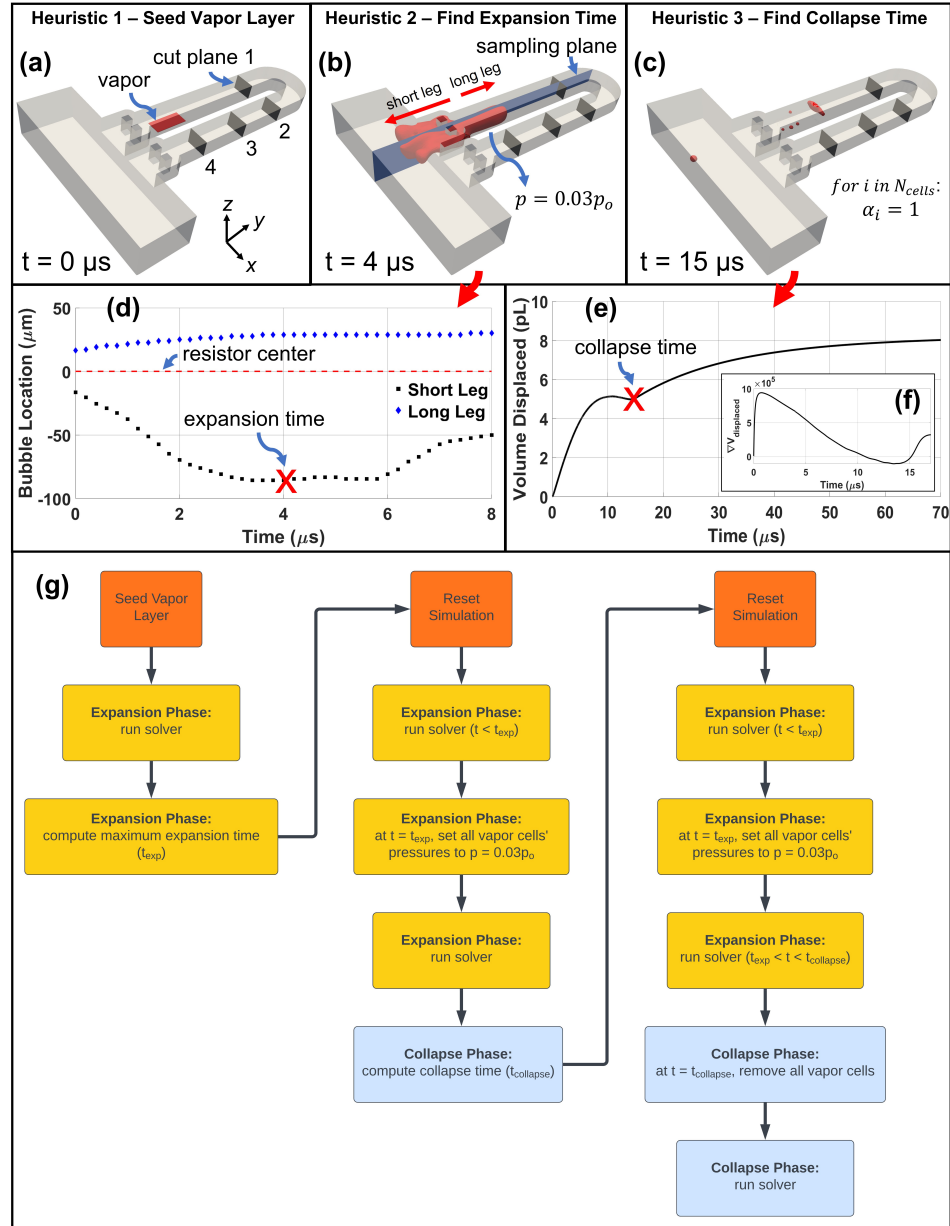


FIG. 1. Model Heuristics. Pre-collapse and post-collapse heuristics are depicted. In (a), thermal bubble nucleation is represented by a seed vapor layer of initial thickness, pressure, and temperature. In (b), the maximum bubble extent is used to find the expansion time in (d) upon which all vapor cells are set to sub-atmospheric pressure,  $p = 0.03p_o$  where  $p_o$  is atmospheric pressure. In (c), the point of bubble collapse is used to find the collapse time in (e) by computing the gradient of the volume displaced over time shown in inset (f). The collapse time is defined as the time at which the gradient of the volume displaced first transitions from negative to positive, here the collapse time is at  $t = 15 \mu\text{s}$ . At the collapse time, all vapor cells are turned to liquid to simulate vapor “dissolution”. In (g), the automated model heuristics are detailed with a flowchart.

This is the author's peer reviewed, accepted manuscript. However, the online version of record will be different from this version once it has been copyedited and typeset.

PLEASE CITE THIS ARTICLE AS DOI: 10.1063/5.0155615

Accepted to Phys. Fluids 10.1063/5.0155615

An OpenFOAM Framework to Model Thermal Bubble-Driven Micro-Pumps

7

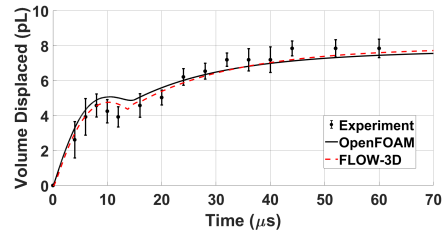


FIG. 2. OpenFOAM Model Validation. Illustrates the cumulative volume displaced per pulse of OpenFOAM model data in comparison to FLOW-3D<sup>23</sup> and experimental data<sup>11</sup> (republished with permission from Goyadinov et al., *Microfluid. Nanofluid.* **20**, 73 (2016). Copyright 2016 Author(s), licensed under a Creative Commons Attribution (CC BY) license). OpenFOAM input parameters for a 0.625  $\mu\text{m}$  grid resolution were:  $t_b = 454 \text{ nm}$ ,  $p_b = 113 p_o$ , and  $T_b = 557 \text{ K}$  where  $t_b$  is the initial vapor layer thickness,  $p_b$  is the initial vapor layer pressure,  $p_o$  is atmospheric pressure,  $T_b$  is the initial vapor layer temperature. Flow rate was measured at cut plane 1 in figure 1. Computation time was 80 and 240 core hours for OpenFOAM and FLOW-3D models respectively.

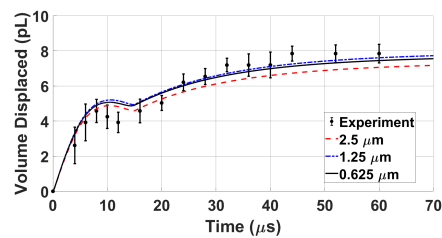


FIG. 3. Mesh Analysis. Mesh analysis study using 0.625, 1.25, and 2.5  $\mu\text{m}$  grid cell resolutions showing convergence to experimental data<sup>11</sup> (republished with permission of the authors). Flow rate was measured at cut plane 1 in figure 1.

This is the author's peer reviewed, accepted manuscript. However, the online version of record will be different from this version once it has been copyedited and typeset.

PLEASE CITE THIS ARTICLE AS DOI: 10.1063/5.0155615

Accepted to Phys. Fluids 10.1063/5.0155615

An OpenFOAM Framework to Model Thermal Bubble-Driven Micro-Pumps

8

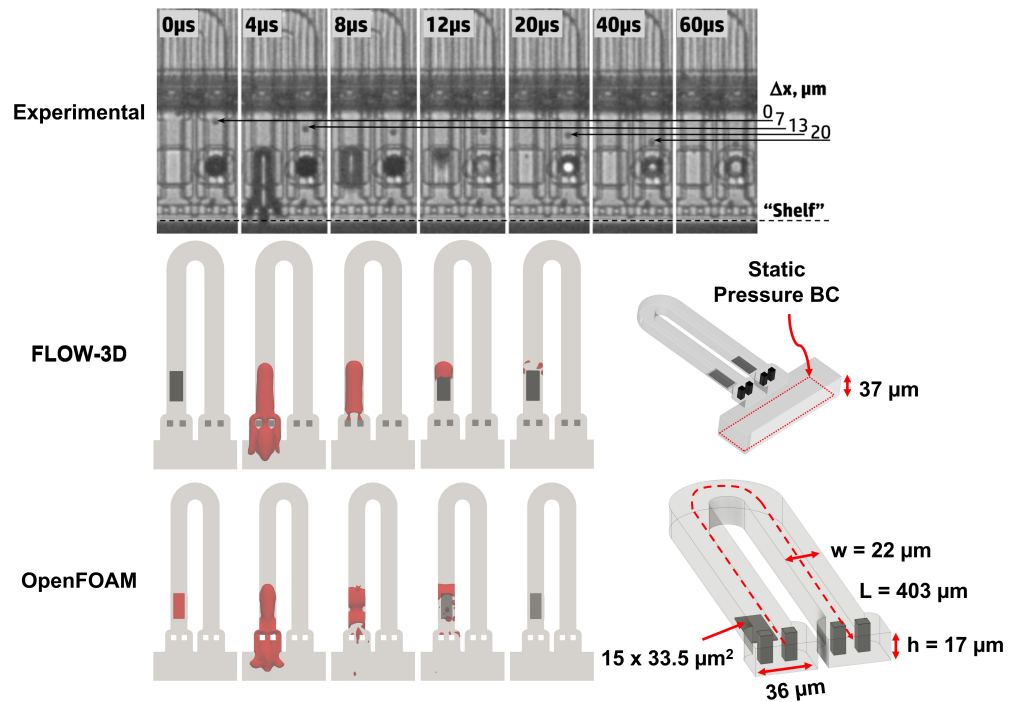


FIG. 4. Top-Down OpenFOAM Bubble Dynamics Validation. OpenFOAM top-down bubble dynamics are compared to experimental data<sup>11</sup> and FLOW-3D simulation results<sup>23</sup> at discrete time steps. Experimental images adapted from Govyadinov et al., “Single-pulse dynamics and flow rates of inertial micropumps”, *Microfluidics and Nanofluidics*, **20**, 73, 2016; licensed under a Creative Commons Attribution (CC BY) license<sup>11</sup>. The U-shaped channel geometry was matched with that used for experimental bubble dynamics data<sup>11</sup> where  $L = 403 \mu\text{m}$ ,  $W = 22 \mu\text{m}$ , and  $H = 17 \mu\text{m}$  for a  $15 \times 33.5 \mu\text{m}^2$  resistor placed  $43 \mu\text{m}$  from the reservoir. No-slip boundary conditions ( $\mathbf{u} = 0$ ) were applied to all boundaries except the bottom of the reservoir in which a static pressure boundary condition ( $p = p_o$ ) was applied. OpenFOAM input parameters were:  $t_b = 454 \text{ nm}$ ,  $p_b = 113 p_o \text{ atm}$ , and  $T_b = 557 \text{ K}$ .

This is the author's peer reviewed, accepted manuscript. However, the online version of record will be different from this version once it has been copyedited and typeset.

PLEASE CITE THIS ARTICLE AS DOI: 10.1063/5.0155615

Accepted to Phys. Fluids 10.1063/5.0155615

An OpenFOAM Framework to Model Thermal Bubble-Driven Micro-Pumps

9

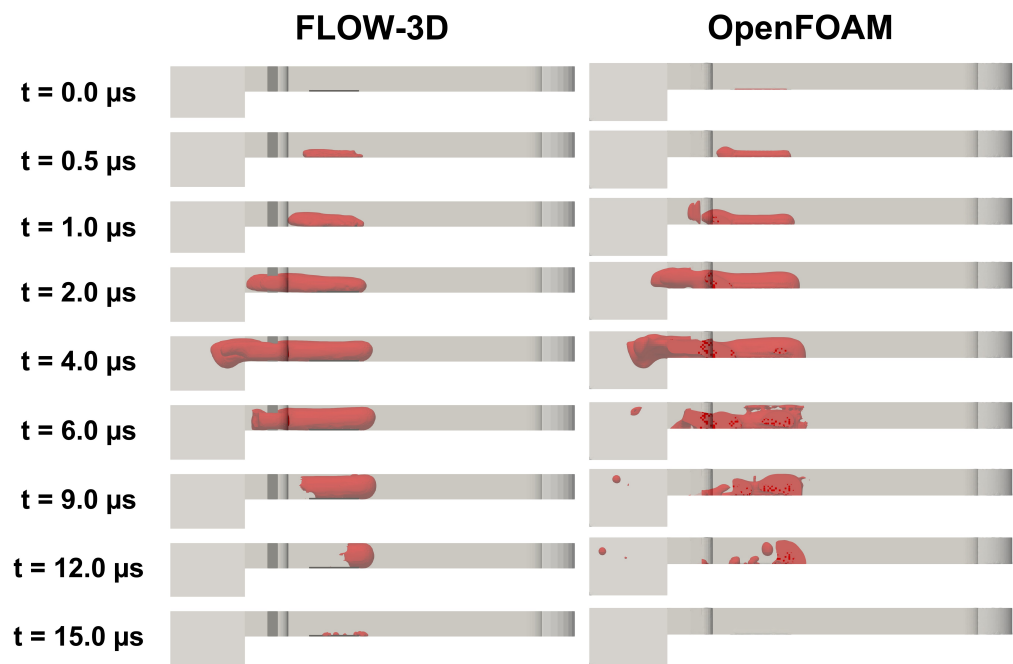


FIG. 5. Side-View OpenFOAM Bubble Dynamics Validation. OpenFOAM side-view bubble dynamics are compared to FLOW-3D simulation results<sup>23</sup> at discrete time steps. OpenFOAM input parameters were:  $t_b = 454 \text{ nm}$ ,  $p_b = 113p_o \text{ atm}$ , and  $T_b = 557 \text{ K}$ .

### III. TRANSIENT FLOW PROFILE ANALYSIS

Thermal bubble-driven micro-pumps can generate net flow with no static pressure head; however, to date, no work has investigated the shape of the velocity profile throughout a pump cycle. Although previous experimental and CFD modeling works show that the net fluid displacement matches that from a fully developed Poiseuille flow profile with deviations around 2-3% at any point on the cross-section<sup>27,28,30</sup>, the shape of the velocity profile throughout the pump cycle can be quite different from theoretical Poiseuille flow in a rectangular channel. Here, we compare the theoretical fully developed Poiseuille velocity profile for flow in a rectangular channel to that from both OpenFOAM and FLOW-3D simulations to assess the transient flow profile shape during both pre-collapse and post-collapse pump stages.

#### A. Theoretical Poiseuille Flow in a Rectangular Channel

Consider fully developed flow along the y-direction of a rectangular channel of width, a, and height, b, which represent the x and z axis respectively. The velocity profile is described by

$$\frac{\partial^2 V_y}{\partial x^2} + \frac{\partial^2 V_y}{\partial z^2} = -\frac{\Delta p}{\mu L} \quad (15)$$

where  $V_y(x, z)$  is the flow profile in the y direction,  $\Delta p$  is the pressure difference,  $\mu$  is the viscosity, and  $L$  is the channel length. From this Poisson's equation, the series solution for the velocity profile is given by the following expressions<sup>38</sup>:

$$V_y(x, z) = \frac{\Delta p}{\mu L} \frac{16}{ab} \sum_{n,m=0}^{\infty} \frac{\sin(p_{2n+1}x)\sin(q_{2m+1}z)}{p_{2n+1}q_{2m+1}(p_{2n+1}^2 + q_{2m+1}^2)} \quad (16)$$

where

$$p_{2n+1} = \frac{\pi(2n+1)}{a} \quad (17)$$

$$q_{2m+1} = \frac{\pi(2m+1)}{b} \quad (18)$$

The velocity profile can be re-written in terms of the average velocity,  $\langle v \rangle = Q/A$ ,

$$V_y(x, z) = \langle v \rangle \frac{ab}{4S_1} \sum_{n,m=0}^{\infty} \frac{\sin(p_{2n+1}x)\sin(q_{2m+1}z)}{p_{2n+1}q_{2m+1}(p_{2n+1}^2 + q_{2m+1}^2)} \quad (19)$$

where

$$S_1(a, b) = \sum_{n,m=0}^{\infty} \frac{1}{p_{2n+1}q_{2m+1}(p_{2n+1}^2 + q_{2m+1}^2)}. \quad (20)$$

Furthermore, following the approach by Kornilovitch et al. for calculation of the average velocity in a rectangular channel<sup>28</sup>, there is a one-to-one correspondence between the maximum to average velocity given by:

$$\frac{v_{max}}{\langle v \rangle} = \frac{3}{2} \cdot \frac{1 - \frac{32}{\pi^3} S_4(a, b)}{1 - \frac{192}{\pi^5} (\frac{b}{a}) S_3(a, b)} \quad (21)$$

where

$$S_3(a, b) = \sum_{m=0}^{\infty} \frac{1}{(2m+1)^5} \frac{\tanh \frac{\pi a(2m+1)}{2b}}{2b} \quad (22)$$

$$S_4(a, b) = \sum_{m=0}^{\infty} \frac{(-1)^m}{(2m+1)^3} \frac{\cosh \frac{\pi a(2m+1)}{2b}}{2b}. \quad (23)$$

Evaluating equation 19 and normalizing to the maximum velocity, figure 6 shows the steady-state velocity profile for fully developed flow in a rectangular channel of width x height,  $22 \times 17 \mu\text{m}^2$ .

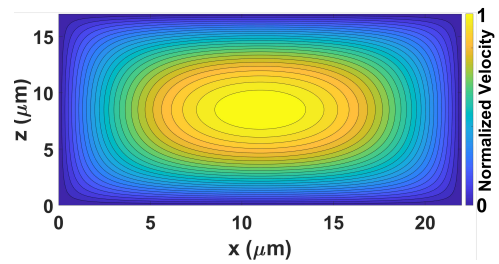


FIG. 6. Theoretical Rectangular Flow Profile. Shows the theoretical velocity profile normalized to the maximum velocity for a width x height,  $22 \times 17 \mu\text{m}^2$  rectangular channel computed using equation 19.

#### B. Simulated Micro-Pump Velocity Profile with Comparison to Theoretical Poiseuille Flow

Thermal bubble-driven micro-pumps create flow that is inherently transient and pulsatile unlike Poiseuille flow which assumes the flow is laminar, steady, and fully developed. Nevertheless, it is common practice to approximate the *per pulse* flow profile with Poiseuille flow in a rectangular channel<sup>13,18,27,28,30</sup>. Here, we compare the simulated velocity profile over a single pump cycle to theoretical Poiseuille flow in a rectangular channel to assess the accuracy of this approximation.

Once the theoretical flow profile is known, the difference between the theoretical velocity profile, shown in figure 6, for a width x height,  $22 \times 17 \mu\text{m}^2$  as used in this study, rectangular channel and the corresponding velocity profiles from OpenFOAM and FLOW-3D simulations throughout one pump cycle is assessed. For each time step in both OpenFOAM and FLOW-3D simulations, the simulation average velocity was used to generate the theoretical flow profile. Moreover, to better estimate the simulation average velocity, the maximum y-velocity was taken and the one-to-one correspondence to the average velocity, equation 21, was used to compute the simulation average velocity at each time step. The absolute average percent error between the theoretical

and simulation velocity profiles was then computed for each time step as described below,

$$error = 100 \times \frac{1}{nm} \sum_{i=1}^n \sum_{j=1}^m \frac{|v_t(x_i, z_j) - v_s(x_i, z_j)|}{v_t(x_i, z_j)} \quad (24)$$

where  $v_t(x_i, z_j)$  is the theoretical velocity profile interpolated at point  $(x_i, z_j)$ ,  $v_s(x_i, z_j)$  is the simulated velocity profile interpolated at point  $(x_i, z_j)$ ,  $n$  is the total number of points along the  $x$  direction, and  $m$  is the total number of points along the  $z$  direction. Figure 7 illustrates the absolute average percent error between the theoretical and simulation velocity profiles taken at cut plane 1 in figure 1a over a full pump cycle for both OpenFOAM and FLOW-3D simulations. During pre-collapse, the vapor bubble expansion and collapse causes large deviations from the theoretical velocity profile. After the vapor bubble fully collapses, at  $t = 15 \mu s$ , the velocity profile more closely matches theoretical Poiseuille flow with an absolute average percent error within 25% for the majority of the post-collapse pump stage.

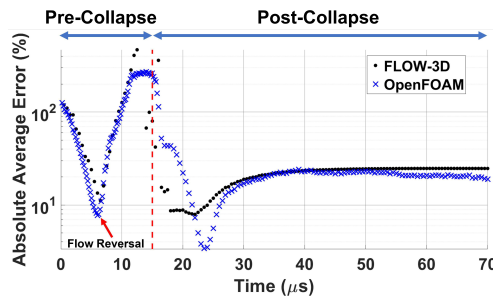


FIG. 7. Absolute Average Percent Error in the Transient Velocity Profile. Illustrates the absolute average percent error between the theoretical and simulation velocity profiles of both OpenFOAM and FLOW-3D for flow in the U-shaped channel taken at cut plane 1 shown in figure 1a. The mesh resolutions for OpenFOAM and FLOW-3D simulations were  $0.625 \mu m$  and  $0.5 \mu m$  respectively. The dashed red line indicates the point of bubble collapse at  $t = 15 \mu s$ .

To better understand the shape of the velocity profile over a single pumping event, cut planes along the channel, see figure 1, were taken. Close to the vapor bubble, the fluid accelerates along all axes in the  $x$ ,  $y$ , and  $z$  directions; however, further down the channel, fluid is directed solely along the channel axis. Thus, cut planes 1-4 are used to ensure the flow profile is monitored far enough away from the vapor bubble to neglect  $x$  and  $z$ -components of the velocity. It was found that cut planes 1-4 all are far enough away from the bubble to neglect  $x$  and  $z$ -components of the velocity. Therefore, only cut plane 1 is analyzed here for brevity.

Figure 8 shows the evolution of both OpenFOAM and FLOW-3D velocity profiles over time, using the  $y$ -component of velocity across cut plane 1. Initially, fluid begins at rest. After bubble nucleation, the high pressure vapor bubble

rapidly accelerates fluid in the channel. Since the boundary layer has yet to fully develop, fluid moves as a slug through the channel,  $t = 1 \mu s$  in figure 8. As fluid moves through the channel, the boundary layer continues to grow,  $t = 4 \mu s$ , until the flow becomes nearly fully developed at  $t = 8 \mu s$ . The long leg of the vapor bubble then reverses direction and collapses which accelerates fluid in the reverse direction and causes flow reversal to occur,  $t = 11 \mu s$ . At this point, fluid in the center of the channel is flowing the fastest and continues to move in the  $+y$  direction while slower moving fluid near the channel walls moves in the reverse  $-y$  direction. As the vapor bubble continues to collapse, fluid eventually fully reverses direction and moves entirely in the  $-y$  direction,  $t = 13 \mu s$ , until the long leg collides with the short leg at  $t = 15 \mu s$ . At the point of complete bubble collapse, fluid in the short leg of the channel has a greater momentum than that in the long leg and thus, post-collapse, fluid is accelerated along the channel axis until it is brought to rest by viscosity. Post-collapse flow,  $t = 18$  and  $30 \mu s$ , closely resembles fully developed Poiseuille flow but does not fully match the shape of the theoretical flow profile which is discussed in the next section.

### C. Violations of Poiseuille Flow and Hydrodynamic Entrance Length Effects

The assumptions of Poiseuille flow is that flow is laminar, steady, and fully developed. From figure 10d, the maximum Reynolds number during the pump cycle is approximately 60; as such, flow can be safely considered laminar throughout the pump cycle. However, it is clear that the flow is not steady. The high pressure vapor bubble expands and collapses which imparts a time dependent, high frequency pressure gradient to the flow closely resembling a delta function. Specifically, figure 9 depicts the fluid average absolute pressure over time simulated in FLOW-3D across cut plane 1, shown in figure 1a. The inlet/outlet pressure is atmospheric pressure. Initially, the high pressure vapor bubble rapidly accelerates the fluid and generates a large pressure gradient driving fluid flow,  $t < 5 \mu s$ . As the vapor bubble expands, its internal pressure quickly drops to sub-atmospheric pressure upon which the vapor bubble collapses. During the collapse stage, the pressure gradient drives bubble collapse until the bubble fully collapses,  $t = 15 \mu s$ , which results in a rapid drop in pressure indicative of post-collapse cavitation that agrees with experimental imaging<sup>11,18</sup>. After the post-collapse cavitation event, the pressure gradient becomes 0,  $t > 20 \mu s$  and fluid is driven by inertia until viscosity brings the fluid to rest.

The last key assumption of Poiseuille flow is that the flow is fully developed. In realistic transient flows, it takes a certain amount of distance along the channel, and thus time, for the boundary layer to fully develop. The distance the fluid has to travel before the boundary layer becomes fully developed is the hydrodynamic entrance length, denoted  $L_e$  as described in figure 10a. In the case of thermal bubble-driven micro-pumps, the hydrodynamic entrance length is a function of time since the velocity varies over a pump cycle. Consider

This is the author's peer reviewed, accepted manuscript. However, the online version of record will be different from this version once it has been copyedited and typeset.

PLEASE CITE THIS ARTICLE AS DOI: 10.1063/5.0155615

Accepted to Phys. Fluids 10.1063/5.0155615

An OpenFOAM Framework to Model Thermal Bubble-Driven Micro-Pumps

12

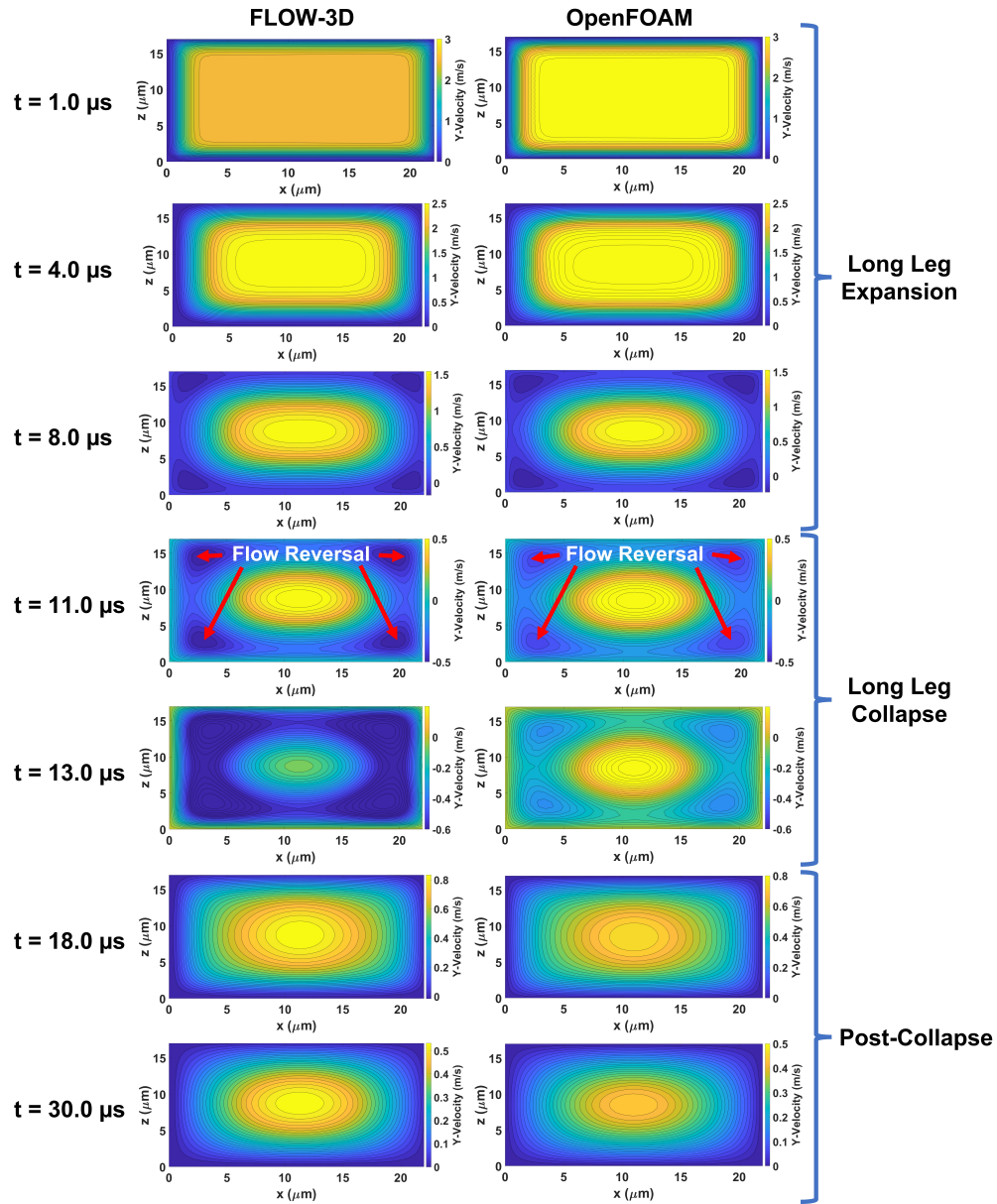


FIG. 8. Transient Velocity Profile over a Single Pumping Event. Illustrates the evolution of the velocity profile in the y direction during a single pumping event for both OpenFOAM and FLOW-3D simulations. The pumping event was broken down into 3 stages: long leg expansion ( $t = 1, 4, \text{ and } 8 \mu\text{s}$ ) in which the vapor bubble is expanding, long leg collapse ( $t = 11 \text{ and } 13 \mu\text{s}$ ) in which the vapor bubble is collapsing, and post-collapse ( $t = 18 \text{ and } 30 \mu\text{s}$ ) in which the vapor bubble re-dissolves back into the fluid.

the evolution of the boundary layer over a single pump cycle of a thermal bubble-driven micro-pump. Initially, fluid begins at rest. After bubble nucleation, fluid is accelerated rapidly and the boundary layer begins to form, as shown in figure 8 at  $t = 1, 4, \text{ and } 8 \mu\text{s}$ . As the boundary layer develops, the flow profile becomes increasingly Poiseuille-like,  $t < 8 \mu\text{s}$  in figure 7 where the absolute average percent error is monotonically decreasing, up until the vapor bubble collapses causing flow reversal which leads to drastic deviations from Poiseuille flow. Once the vapor bubble fully collapses,  $t = 15 \mu\text{s}$ , momentum imbalance drives fluid flow upon which the boundary layer re-develops. During post-collapse, fluid moves with a decaying velocity until viscosity brings the fluid to rest. However, even during the post-collapse stage, flow never fully matches theoretical Poiseuille flow; instead, the absolute average percent error is approximately 25% during the post-collapse stage. We hypothesize that the transient nature of flow during a single pump cycle of thermal bubble-driven micro-pumps results in a dynamic boundary layer in which fluid never travels the required entrance length to become fully developed. Thus, it cannot be expected for theoretical Poiseuille flow to perfectly match the flow profile of thermal bubble-driven micro-pumps even during the post-collapse stage.

Commonly, hydrodynamic entrance length analysis describes steady flows. In fact, there is a large body of research analyzing the hydrodynamic entrance length of various channel geometries across a range of Reynolds numbers and aspect ratios<sup>39-41</sup>. In contrast, for transient flows in which the boundary layer can be dynamic, describing the hydrodynamic entrance length is more challenging. There exist both an entrance length and a required time for the flow to develop, termed the “development time.” Chaudhury et al. studied starting flows in a finite length tube for Reynolds numbers of 500 - 3000 and found that the hydrodynamic entrance length needed to achieve fully developed transient flow is approximately equal to the hydrodynamic entrance length needed to achieve fully developed steady flow<sup>42</sup>. Although the maximum Reynolds number for flow during a single pump cycle of thermal bubble-driven micro-pumps is approximately 60, shown in figure 10d, we use the analysis from Chaudhury et al. to provide a first order approximation of how the transient flow develops over a single pump cycle of a thermal bubble-driven micro-pump. Moreover, we utilize the following empirical hydrodynamic entrance length relation for steady flow in a rectangular micro-channel to estimate the required hydrodynamic entrance length throughout a single pump cycle of a thermal bubble-driven micro-pump<sup>43</sup>:

$$\mathcal{L}_e = \frac{L_e}{W} = \left( C_1^{C_3} + (C_2 Re)^{C_3} \right)^{\frac{1}{C_3}} \quad (25)$$

where

$$C_1 = 0.7 \left( \frac{H}{W} \right)^{\frac{1}{4}} \quad (26)$$

$$C_2 = \frac{6.8 \left( \frac{H}{W} \right)^{3.75}}{1 + 90 \left( \frac{H}{W} \right)^{2.8}} \quad (27)$$

$$C_3 = 1 + \left( \frac{H}{W} \right) \quad (28)$$

for  $0 < Re < 2000$  and  $0.1 < \frac{H}{W} < 1$ . Here,  $\frac{H}{W}$  is the channel aspect ratio. In this study, the channel aspect ratio is 0.77. Figure 10b describes the absolute distance the fluid travels during a pump cycle.  $\Delta d_1$  and  $\Delta d_2$  are the pre-collapse and post-collapse absolute distance traveled, which is 14.4 and 8.4  $\mu\text{m}$  respectively. In comparison to figure 10c which evaluates equation 25 as a function of time throughout the pump cycle, it is evident that higher fluid velocities, which occur during the pre-collapse stage, require a longer distance the fluid must travel before the boundary layer fully develops. During pre-collapse, the fluid travels an absolute distance of  $\Delta d_1 = 14.4 \mu\text{m}$  which is less than the average hydrodynamic entrance length over the pre-collapse stage,  $\langle L_e \rangle_{pre} = 44.4 \mu\text{m}$ . Thus, during pre-collapse, it is expected that the flow never becomes fully developed. Similarly, during post-collapse, the fluid travels an absolute distance of  $\Delta d_2 = 8.4 \mu\text{m}$  which is less than the average hydrodynamic entrance length over the post-collapse stage,  $\langle L_e \rangle_{post} = 16.1 \mu\text{m}$ . Therefore, during both pre-collapse and post-collapse stages, the flow is not expected to become fully developed. We find that the transient shape of the flow profile deviates greatly from theoretical Poiseuille flow during pre-collapse and more closely resembles theoretical Poiseuille flow during post-collapse.

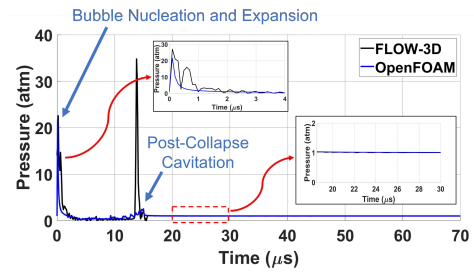


FIG. 9. Transient Average Absolute Pressure across Cut Plane 1. Illustrates the average absolute pressure over time simulated in FLOW-3D and OpenFOAM across cut plane 1 in figure 1a. The bubble nucleation and expansion as well as post-collapse cavitation points are highlighted. The inset images illustrate zoomed in sections of the data from 0-4  $\mu\text{s}$  and 18-30  $\mu\text{s}$ . Fluid pressure becomes atmospheric pressure immediately after post-collapse which results in no pressure gradient driving the flow; thus, fluid is driven by its inertia until viscosity brings the fluid to rest. Data output time step was 100 ns and data was filtered using a moving mean filter of 3 time steps.

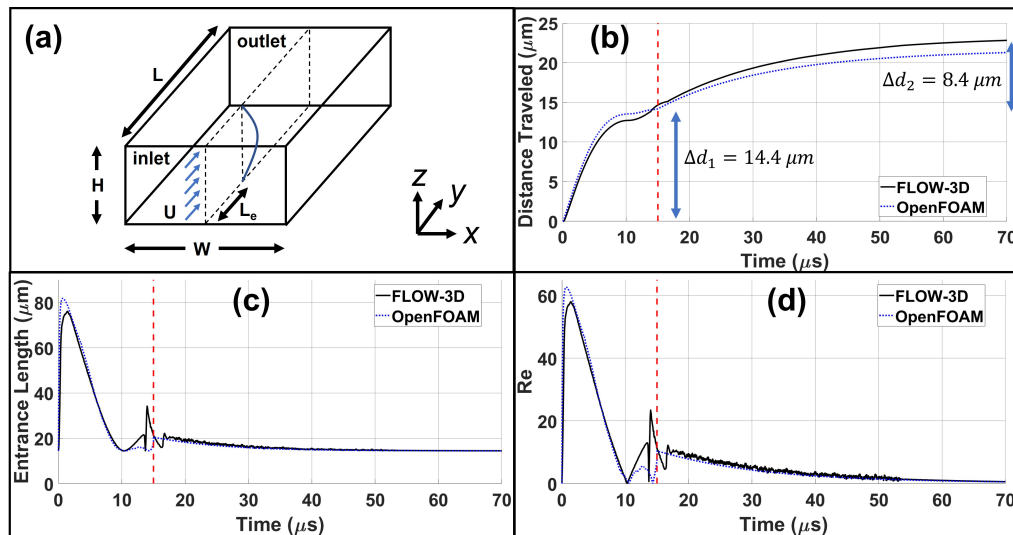


FIG. 10. Entrance Length Effect of Thermal Bubble-Driven Micro-Pumps. (a) Illustrates the hydrodynamic entrance length effect for flow in a rectangular channel. (b-d) Analyze flow in the U-shaped channel shown in figure 1a. (b) Shows the absolute distance traveled by the fluid over a single pump cycle where  $\Delta d_1$  and  $\Delta d_2$  are the pre-collapse and post-collapse net distance traveled respectively. The dashed red line indicates the point of bubble collapse,  $t = 15 \mu s$ . (c) Depicts the hydrodynamic entrance length as a function of time over a single pump cycle. (d) Depicts the Reynolds number as a function of time over a single pump cycle.

#### IV. CONCLUSIONS

The present study details an open source OpenFOAM framework to model thermal bubble-driven micro-pumps. The developed OpenFOAM model enables prediction of the flow rate as well as bubble dynamics for thermal bubble-driven micro-pumps without the need for expensive commercial software and can take advantage of high-performance computing (HPC) clusters. Pre-collapse and post-collapse flow and bubble dynamics were resolved through the application of physics-based model heuristics. The OpenFOAM model was validated and is in agreement with both experimental and FLOW-3D data. The developed OpenFOAM framework provides significant time savings (3X) over full multiphysics CFD solvers such as FLOW-3D where a single  $70 \mu s$  pump event took 80 core hours to simulate for the OpenFOAM model compared to 240 core hours for FLOW-3D. Furthermore, the shape of the transient velocity profile over a pump cycle was analyzed for the first time. It was found that the velocity profile deviates substantially from fully developed Poiseuille flow during the pre-collapse stage of the pump cycle but closely resembles fully developed Poiseuille flow during the post-collapse stage. Furthermore, it was found that flow does not become fully developed over the pump cycle; as such, deviations between theoretical Poiseuille flow and the transient velocity profile should be expected when using thermal bubble-driven micro-pumps.

To date, no readily available open source CFD tools exist to model both the pre-collapse and post-collapse stages of thermal bubble-driven micro-pumps. As such, this work provides an OpenFOAM framework to model, understand, and optimize microfluidic systems with thermal bubble-driven micro-pumps. We envision that the developed OpenFOAM framework will be an important tool for microfluidic designers and researchers to simulate devices with thermal bubble-driven micro-pumps.

This is the author's peer reviewed, accepted manuscript. However, the online version of record will be different from this version once it has been copyedited and typeset.

PLEASE CITE THIS ARTICLE AS DOI: 10.1063/5.0155615

Accepted to *Phys. Fluids* 10.1063/5.0155615

An OpenFOAM Framework to Model Thermal Bubble-Driven Micro-Pumps

15

#### ACKNOWLEDGMENTS

The authors would like to thank Pavel Kornilovitch, Alex Govyadinov, Debanjan Mukherjee, and Nathalie Vriend for insights and fruitful discussions of this work.

Experimental image in figure 4 adapted from Govyadinov et al., "Single-pulse dynamics and flow rates of inertial micropumps", *Microfluidics and Nanofluidics*, **20**, 73, 2016; licensed under a Creative Commons Attribution (CC BY) license<sup>11</sup>.

This work utilized the Alpine supercomputer<sup>44</sup>, which is jointly funded by the University of Colorado Boulder, the University of Colorado Anschutz, Colorado State University, and the National Science Foundation (award 2201538).

This material is based upon work supported by the National Science Foundation Graduate Research Fellowship under Grant No. DGE 1650115. Any opinion, findings, and conclusions or recommendations expressed in this material are those of the author(s) and do not necessarily reflect the views of the National Science Foundation.

#### DATA AVAILABILITY

The data that support the findings of this study are available from the corresponding author upon reasonable request.

REFERENCES

- <sup>1</sup>N. Mishchuk, T. Heldal, T. Volden, J. Auerswald, and H. Knapp, "Micropump based on electroosmosis of the second kind," *Electrophoresis* **30** (2009).
- <sup>2</sup>J. Snyder, J. Getprecharsawas, D. Fang, T. Gaborski, C. Striemer, P. Fauchet, D. Borkholder, and J. McGrath, "High-performance, low-voltage electroosmotic pumps with molecularly thin silicon nanomembranes," *Proceedings of the National Academy of Sciences* **110**, 18425–18430 (2013), <https://www.pnas.org/content/110/46/18425.full.pdf>.
- <sup>3</sup>Q. Shizhi and H. Bau, "Magneto-hydrodynamics based microfluidics," *Mechanics Research Communications* **36** (2009).
- <sup>4</sup>D. Duffy, H. Gillis, J. Lin, N. Sheppard, and G. Kellogg, "Microfabricated centrifugal microfluidic systems: Characterization and multiple enzymatic assays," *Analytical Chemistry* **71** (1999).
- <sup>5</sup>K. Vinayakumar, G. Nadiger, V. Shetty, S. Dinesh, M. Nayak, and K. Rajanna, "Packaged peristaltic micropump for controlled drug delivery application," *Review of Scientific Instruments* **88** (2017).
- <sup>6</sup>T. Ma, S. Sun, B. Li, and J. Chu, "Piezoelectric peristaltic micropump integrated on a microfluidic chip," *Sensors and Actuators A: Physical* **292**, 90–96 (2019).
- <sup>7</sup>S. Hassan and X. Zhang, "Design and fabrication of capillary-driven flow device for point-of-care diagnostics," *Biosensors* **39** (2020).
- <sup>8</sup>E. Torniainen, A. Goyadinov, D. Markel, and P. Kornilovitch, "Bubble-driven inertial micropump," *Physics of Fluids* **24** (2012).
- <sup>9</sup>M. I. Mohammed, S. Haswell, and I. Gibson, "Lab-on-a-chip or chip-in-a-lab: Challenges of commercialization lost in translation," *Procedia Technology* **20**, 54–59 (2015), proceedings of The 1st International Design Technology Conference, DESTECH2015, Geelong.
- <sup>10</sup>M. Einat and M. Grajower, "Microboiling measurements of thermal-inkjet heaters," *Journal of Microelectromechanical Systems* **19** (2010).
- <sup>11</sup>A. Goyadinov, P. Kornilovitch, D. Markel, and E. Torniainen, "Single-pulse dynamics and flow rates of inertial micropumps," *Microfluidics and Nanofluidics* **20** (2016).
- <sup>12</sup>B. Hayes, A. Hayes, M. Rolleston, A. Ferreira, and J. Kirsher, "Pulsatory mixing of laminar flow using bubble-driven micro-pumps," *Proceedings of the ASME 2018 International Mechanical Engineering Congress and Exposition* **7** (2018).
- <sup>13</sup>B. Hayes, A. Goyadinov, and P. Kornilovitch, "Microfluidic switchboards with integrated inertial pumps," *Microfluidics and Nanofluidics* **22** (2018).
- <sup>14</sup>H. Hoefemann, S. Wadle, N. Bakhtina, V. Kondrashov, N. Wangler, and R. Zengerle, "Sorting and lysis of single cells by bubblejet technology," *Sensors and Actuators B: Chemical* **168**, 442–445 (2012).
- <sup>15</sup>D. van den Broek and M. Elwenspoek, "Explosive micro-bubble actuator," *Sensors and Actuators A: Physical* **145-146**, 387–393 (2008), special Issue: Transducers/07 Eurosensors XXI, The 14th International Conference on Solid State Sensors, Actuators and Microsystems and the 21st European Conference on Solid-State Transducers.
- <sup>16</sup>B. Liu, Y. Hou, D. Li, and J. Yang, "A thermal bubble micro-actuator with induction heating," *Sensors and Actuators A: Physical* **222**, 8–14 (2015).
- <sup>17</sup>K. Okuyama, S. Mori, K. Sawa, and Y. Iida, "Dynamics of boiling succeeding spontaneous nucleation on a rapidly heated small surface," *International Journal of Heat and Mass Transfer* **49**, 2771–2780 (2006).
- <sup>18</sup>B. Hayes, L. Smith, H. Kabutz, A. C. Hayes, G. L. Whiting, K. Jayaram, and R. MacCurdy, "Rapid fabrication of low-cost thermal bubble-driven micro-pumps," *Micromachines* **13** (2022), 10.3390/mi13101634.
- <sup>19</sup>Y. Qu and J. Zhou, "Lumped parameter model and numerical model of vapor bubble-driven valve-less micro-pump," *Advances in Mechanical Engineering* **9**, 1687814017695958 (2017), <https://doi.org/10.1177/1687814017695958>.
- <sup>20</sup>*CFD Model of the Thermal Inkjet Droplet Ejection Process*, Heat Transfer Summer Conference, Vol. 3 (2007).
- <sup>21</sup>H. Zhou and A. Gué, "Simulation model and droplet ejection performance of a thermal-bubble microjector," *Sensors and Actuators B: Chemical* **145**, 311–319 (2010).
- <sup>22</sup>Y. Hong, N. Ashgriz, J. Andrews, and H. Parizi, "Numerical simulation of growth and collapse of a bubble induced by a pulsed microheater," *Journal of Microelectromechanical Systems* **13**, 857–869 (2004).
- <sup>23</sup>B. Hayes, G. L. Whiting, and R. MacCurdy, "Modeling of contactless bubble-bubble interactions in microchannels with integrated inertial pumps," *Physics of Fluids* **33**, 042002 (2021), <https://doi.org/10.1063/5.0041924>.
- <sup>24</sup>Z. Yin and A. Prosperetti, "'blinking bubble' micropump with micro-fabricated heaters," *Journal of Micromechanics and Microengineering* **15** (2005).
- <sup>25</sup>E. Ory, H. Yuan, A. Prosperetti, S. Popinet, and S. Zaleski, "Growth and collapse of a vapor bubble in a narrow tube," *Physics of Fluids* **12** (2000).
- <sup>26</sup>H. Yuan and A. Prosperetti, "The pumping effect of growing and collapsing bubbles in a tube," *Journal of Micromechanics and Microengineering* **9**, 402–413 (1999).
- <sup>27</sup>P. Kornilovitch, A. Goyadinov, D. Markel, and E. Torniainen, "One-dimensional model of inertial pumping," *Phys. Rev. E* **87** (2013).
- <sup>28</sup>P. E. Kornilovitch, T. Cochell, and A. N. Goyadinov, "Temperature dependence of inertial pumping in microchannels," *Physics of Fluids* **34**, 022003 (2022), <https://doi.org/10.1063/5.0079327>.
- <sup>29</sup>A. Asai, "Three-Dimensional Calculation of Bubble Growth and Drop Ejection in a Bubble Jet Printer," *Journal of Fluids Engineering* **114**, 638–641 (1992), [https://asmedigitalcollection.asme.org/fluidsengineering/article-pdf/114/4/638/5711867/638\\_1.pdf](https://asmedigitalcollection.asme.org/fluidsengineering/article-pdf/114/4/638/5711867/638_1.pdf).
- <sup>30</sup>H. Tan, E. Torniainen, D. P. Markel, and R. N. K. Browning, "Numerical simulation of droplet ejection of thermal inkjet printheads," *International Journal for Numerical Methods in Fluids* **77**, 544–570 (2015), <https://onlinelibrary.wiley.com/doi/pdf/10.1002/ld.3997>.
- <sup>31</sup>H. Li, J. Huang, X. Wu, J. Zhang, J. Wang, Y. Wang, and C. Huang, "Dynamic behaviors of a laser-induced bubble and transition mechanism of collapse patterns in a tube," *AIP Advances* **10**, 035210 (2020), <https://doi.org/10.1063/1.5142739>.
- <sup>32</sup>M. Koch, J. M. Rosselló, C. Lechner, W. Lauterborn, and R. Mettin, "Dynamics of a laser-induced bubble above the flat top of a solid cylinder – mushroom-shaped bubbles and the fast jet," *Fluids* **7** (2022), 10.3390/fluids7010002.
- <sup>33</sup>J. M. Rosselló, H. Reese, and C.-D. Ohl, "Dynamics of pulsed laser-induced cavities on a liquid–gas interface: from a conical splash to a 'bullet' jet," *Journal of Fluid Mechanics* **939**, A35 (2022).
- <sup>34</sup>Y. Sun, Z. Yao, H. Wen, Q. Zhong, and F. Wang, "Cavitation bubble collapse in a vicinity of a rigid wall with a gas entrapping hole," *Physics of Fluids* **34** (2022), 10.1063/5.0096986, 073314, [https://pubs.aip.org/aip/pof/article-pdf/doi/10.1063/5.0096986/16643026/073314\\_1\\_online.pdf](https://pubs.aip.org/aip/pof/article-pdf/doi/10.1063/5.0096986/16643026/073314_1_online.pdf).
- <sup>35</sup>C. Hirt and B. Nichols, "Volume of fluid (vof) method for the dynamics of free boundaries," *Journal of Computational Physics* **39**, 201–225 (1981).
- <sup>36</sup>J. Brackbill, D. Kothe, and C. Zemach, "A continuum method for modeling surface tension," *Journal of Computational Physics* **100**, 335–354 (1992).
- <sup>37</sup>H. G. Weller, "A new approach to vof-based interface capturing methods for incompressible and compressible flow," *OpenCFD Ltd., Report TR/HGW* **4**, 35 (2008).
- <sup>38</sup>S. Timoshenko and J. Goodier, *Theory of Elasticity*, 3rd ed. (McGraw-Hill, Inc., 1970).
- <sup>39</sup>*Laminar Entrance Length in Microtubes*, Fluids Engineering Division Summer Meeting, Vol. Volume 2: Fora (2009) [https://asmedigitalcollection.asme.org/FEDSM/proceedings-pdf/FEDSM2009/43734/549/2749373/549\\_1.pdf](https://asmedigitalcollection.asme.org/FEDSM/proceedings-pdf/FEDSM2009/43734/549/2749373/549_1.pdf).
- <sup>40</sup>J. Koo and C. Kleinstreuer, "Liquid flow in microchannels: experimental observations and computational analyses of microfluidics effects," *Journal of Micromechanics and Microengineering* **13**, 568 (2003).
- <sup>41</sup>T. Ahmad and I. Hassan, "Experimental Analysis of Microchannel Entrance Length Characteristics Using Microparticle Image Velocimetry," *Journal of Fluids Engineering* **132** (2010), 10.1115/1.4001292, 041102, [https://asmedigitalcollection.asme.org/fluidsengineering/article-pdf/132/4/041102/5517586/041102\\_1.pdf](https://asmedigitalcollection.asme.org/fluidsengineering/article-pdf/132/4/041102/5517586/041102_1.pdf).
- <sup>42</sup>R. A. Chaudhury, M. Herrmann, D. H. Frakes, and R. J. Adrian, "Length and time for development of laminar flow in tubes following a step increase of volume flux," *Experiments in Fluids* **56**, 22 (2015).
- <sup>43</sup>G. Ferreira, A. Suceana, L. L. Ferrás, F. T. Pinho, and A. M. Afonso, "Hydrodynamic entrance length for laminar flow in microchannels with rectangular cross section," *Fluids* **6** (2021), 10.3390/fluids6070240.
- <sup>44</sup>J. Anderson, P. J. Burns, D. Milroy, P. Ruprecht, T. Hauser, and H. J. Siegel, "Deploying rmacc summit: An hpc resource for the rocky mountain region;" in *Proceedings of the Practice and Experience in Advanced Research Computing 2017 on Sustainability, Success and Impact*, PEARC17 (Association for Computing Machinery, New York, NY, USA, 2017).